Proceedings of the Combustion Institute 42 (2026) 106010

Contents lists available at ScienceDirect

Proceedings of the Combustion Institute

journal homepage: www.elsevier.com/locate/proci

Real-time tracking of iron oxide particle reduction with hydrogen in a fluidized bed reactor

Martin P. Kannengießer [a,*], Lukas Braun [b,c], Fabian P. Hagen [a,*], Malte Seitz [a], Leon Mögerle [a], Björn Stelzner [a], Jan-Dierk Grunwaldt [b,c], Dmitry E. Doronkin [b,c], Dimosthenis Trimis [a]

[a] Engler-Bunte-Institute, Combustion Technology, Karlsruhe Institute of Technology (KIT), Engler-Bunte-Ring 7, 76131 Karlsruhe, Germany
[b] Institute for Chemical Technology and Polymer Chemistry, Karlsruhe Institute of Technology (KIT), Engesserstr. 18/20, 76131 Karlsruhe, Germany
[c] Institute of Catalysis Research and Technology, KIT, Hermann-von-Helmholtz-Platz 1, 76344 Eggenstein-Leopoldshafen, Germany

ARTICLE INFO

Keywords:
Fluidized bed reactor
Iron oxide reduction
Hydrogen
X-ray absorption spectroscopy
Synchrotron

ABSTRACT

Reduction of micron-sized Fe_2O_3 particles with hydrogen was investigated in a fluidized bed reactor (FBR), designed and developed as part of this study and equipped with X-ray transparent glassy carbon windows. Simultaneous *in situ* X-ray absorption spectroscopy (XAS) at a synchrotron source and quadrupole mass spectrometry (QMS) enabled correlated real-time monitoring of solid-phase transformations and gas-phase composition during isothermal reduction at 773 K in a 1:1 H_2/N_2 atmosphere. Time-resolved XAS revealed a sequential transformation from Fe_2O_3 to Fe_3O_4 and metallic Fe, while QMS detected a corresponding increase and subsequent decay of H_2O. A systematic temporal offset between solid- and gas-phase signals indicates that the diagnostics probe slightly different particle ensembles: XAS captures particles present in the freeboard, whereas QMS reflects the integrated H_2O formation from the entire reacting bed. Temporary trapping of H_2O within the evolving pore network, previously reported for reducing iron oxide particles, may further contribute to the delayed gas-phase response. No evidence for a persistent FeO phase was observed under the investigated conditions. The reduction proceeds rapidly during the initial stage and subsequently slows down, likely associated with the formation of passivating Fe/Fe_3O_4 layers that limit hydrogen access and hinder the transport of water from the particle core. The present work establishes an experimental framework for synchrotron *operando* studies of iron oxide reduction in fluidized bed reactors, enabling correlated XAS-QMS measurements and providing the basis for upcoming systematic investigations of particle properties, morphologies and operating parameters.

Novelty and significance statement: Braun et al. [1] investigated quasi-single iron oxide reduction in inert-particle-diluted fixed bed reactor cells under low hydrogen concentrations and varying temperatures. While providing kinetic insights, these experiments were limited to the solid phase and did not capture the multi-particle interactions, improved temperature control, or enhanced mass transport characteristic of fluidized bed reactors (FBRs). This work presents real-time tracking of iron oxide reduction with hydrogen in an X-ray absorption spectroscopy (XAS)-compatible FBR designed in this study and operated under practically relevant isothermal conditions. The combination of *in situ* XAS and quadrupole mass spectrometry (QMS) enables, for the first time, simultaneous monitoring of solid- and gas-phase transformations and reveals their correlated evolution during reduction. The XAS-QMS approach addresses the scarcity of *operando* studies in FBRs and is transferable to different reaction conditions, particle properties, and iron ores, extending its relevance from energy storage to steelmaking, materials, and catalysis.

* Corresponding authors.
E-mail addresses: martin.kannengiesser@kit.edu (M.P. Kannengießer), fabian.hagen@kit.edu (F.P. Hagen).

https://doi.org/10.1016/j.proci.2026.106010
Received 15 March 2026; Accepted 5 June 2026

1. Introduction

Micron-sized iron particles have gained attention as carbon-free energy carriers, enabling a Fe–H_2-redox cycle for renewable energy storage systems [2,3]. In this concept, H_2 reduces iron oxide particles to metallic iron, which can then be stored and transported as a stable, non-toxic solid energy carrier over long periods and distances [4,5]. The stored energy can be released upon re-oxidation of the iron when demand arises, producing heat and regenerating the oxides, thus closing the redox cycle [6–8].

Due to their high volumetric energy density and favorable storage and handling characteristics, iron powders are increasingly considered as dispatchable energy carriers alongside hydrogen, ammonia, and synthetic hydrocarbons [9]. System-level and techno-economic analyses indicate competitive round-trip efficiencies and costs, leveraging existing metallurgical and power-generation infrastructure [10,11].

The reduction of iron oxide particles can be performed using various reactor concepts, most notably flash reduction (FR) and fluidized bed reactors (FBR). FR enables rapid reduction of fine particles at high temperature, elevated H_2 concentration and short residence time [12–15]. In FBRs, the upward gas flow suspends and mixes the particles, resulting in a homogeneous temperature distribution and high conversion rates even at temperatures down to 773 K. The reduction can be completed within reasonable time periods, provided that both H_2 partial pressure and fluidization quality are sufficient [16–19]. Optimizing gas-phase composition and flow can mitigate sintering and incomplete conversion, making FBRs well-suited for iron-based renewable energy storage [20–22].

Depending on temperature, the reduction of iron oxides with hydrogen can proceed via two distinct pathways [23]. Above 843 K, the full sequence is

$$\mathrm{Fe_2O_3} \longrightarrow \mathrm{Fe_3O_4} \longrightarrow \mathrm{FeO} \longrightarrow \mathrm{Fe}\,. \tag{1}$$

Below 843 K, bulk FeO becomes thermodynamically unstable and results in the formation of Fe and Fe_2O_3 only, such that the reduction follows the two-step sequence

$$\mathrm{Fe_2O_3} \longrightarrow \mathrm{Fe_3O_4} \longrightarrow \mathrm{Fe}\,. \tag{2}$$

In the present work, the temperature T is restricted to 773 K, which falls below the FeO stability limit. Therefore, the reduction pathway is expected to follow Eq. (2). Each step exhibits distinct kinetic characteristics and potentially different rate-controlling mechanisms [1,23–26]. Recent kinetic studies treat these transformations as consecutive reactions with separate apparent rate coefficients and activation energies, often embedded in shrinking core or grain models to account for intraparticle transport limitations [23,27–29]. Depending on the chosen kinetic model, experimental configuration, and temperature range, the reported reaction parameters vary over a wide range [23], which limits the transferability of kinetic data across reactor configurations and motivates *operando* characterization under process-relevant conditions.

To address these limitations, recent advances in *in situ* and *ex situ* characterization have provided new insight into redox mechanisms and phase transformations [1,24,25,30,31]. These X-ray-based and γ-resonant spectroscopic diagnostics provide a more comprehensive understanding of redox dynamics beyond the surface layer and have significantly advanced insight into the pathways and kinetics of iron oxide reduction, directly supporting process optimization for scalable renewable energy storage applications.

However, most of these mechanistic studies have been performed in small fixed bed reactors, with their insights now informing the development of FBRs. Notably, in this work, the simultaneous application of *in situ* X-ray absorption spectroscopy (XAS) and quadrupole mass spectrometry (QMS) was implemented for the first time in a FBR equipped with X-ray transparent windows, developed as part of this study and operated at the Deutsches Elektronen-Synchrotron (DESY) in Hamburg at the PETRA III beamline P64. While XAS probes the solid-state transformations of iron, QMS monitors the evolving gas-phase composition. Together, these methods provide correlated data linking solid- and gas-phase dynamics during iron oxide reduction with H_2.

2. Methods and materials

This section describes the FBR used for *operando* XAS measurements, the reaction conditions and iron oxide powder investigated in this study, and the diagnostics applied for real-time tracking of the gas and solid phases as well as for *ex situ* analysis.

2.1. XAS-compatible fluidized bed reactor

The FBR used in this study is a downscaled version of the reactor introduced and characterized by Seitz et al. [19]. It features an inner diameter of 50 mm and an effective length of 270 mm, see Fig. 1. The inner diameter was selected as the largest diameter compatible with XAS measurements in transmission mode while still providing sufficient signal quality for reliable linear combination analysis (LCA), see Section 2.4. Preliminary tests further showed that smaller reactor diameters increase the relative influence of the reactor walls and can therefore promote fluidization instabilities and defluidization events.

The bed support consists of two fine mesh grids (15 µm pore size) mounted within the lower flange to ensure uniform gas distribution and retention of micron-sized particles. A powder reservoir is located above the upper flange and connected via a valve controlled feed, allowing solid material to be introduced into the preconditioned reactor during operation.

Two X-ray transmissive windows for XAS measurements are integrated on opposing sides of the reactor wall, enabling an incident and a transmitted beam path. Each window is made of glassy carbon (0.5 mm thickness, 180 mm length, 6 mm width), providing high X-ray transparency and stability under reducing conditions at high temperatures. To prevent oxidation of the window material, a N_2 purge is directed at the outer surfaces. The distance between the mesh support and the window is 35 mm. The FBR is mounted on a linear stage, allowing alignment with the synchrotron X-ray beam.

Gas supply is regulated by thermal mass flow controllers, providing an adjustable mixture of N_2 and H_2 that is preheated before entering the reactor. The reactor is enclosed in a heating jacket capable of maintaining stable operation at temperatures up to 923 K, while an additional heating wire around the lower conical section ensures uniform temperature in this region.

For process monitoring, differential pressure sensors and temperature probes are installed below and above the mesh supports, as well as above the fluidized bed. This arrangement enables the characterization of hydrodynamics and temperature during reactor operation.

2.2. Reaction conditions and iron oxide powder

Fe_2O_3 powder with a median particle diameter d_{50} of approximately 70 µm, also used in [19], was employed in the experiments. Its volume-based particle size distribution (PSD) was measured by laser diffraction and is shown in Fig. 2 as both the cumulative volume distribution $Q_3(d)$ and the corresponding distribution density $q_3(d)$ as functions of the particle diameter d. A scanning electron microscopy (SEM) image of the as-received powder is shown in Fig. 3, while additional powder properties are reported in [19].

In this study, 22 g of Fe_2O_3 powder were introduced into the FBR, resulting in a static bed height of 30 mm, which was selected to match the bed height used in the complementary pilot-scale FBR experiments reported in Ref. [19]. The particles were loaded into the pre-heated reactor at the target temperature to avoid thermally induced morphological changes prior to the reduction reaction. The reduction was conducted at 773 K with a total gas flow rate of 10 l min^{-1} (@273 K, 1 bar) using a 1:1 mixture of H_2 and N_2. The operating conditions were chosen based on pilot-scale FBR experiments with the same iron oxide particles, which showed that stable bubbling fluidization requires operation well above the theoretical minimum fluidization velocity, as commonly observed for cohesive powders [19]. Following

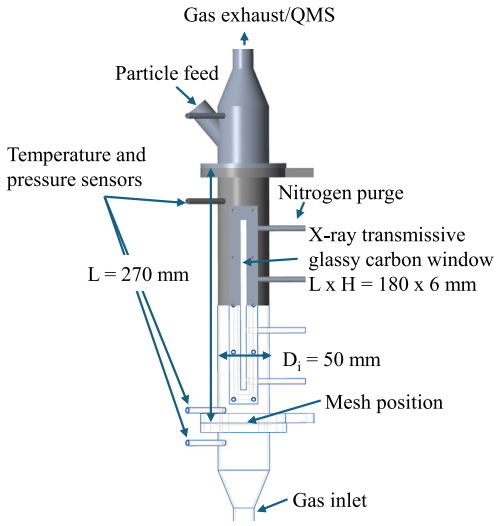

Fig. 1. Schematic of the FBR designed for *operando* XAS measurements.

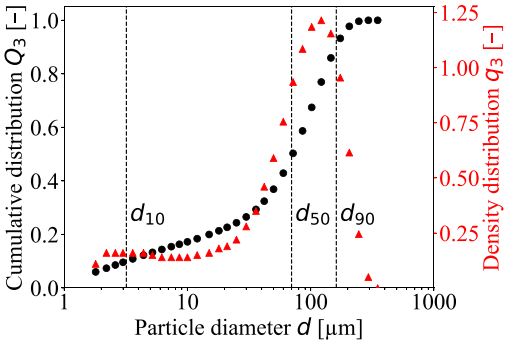

Fig. 2. Volume-based particle size distribution of the Fe_2O_3 powder used in this study, shown as the cumulative distribution $Q_3(d)$ and the density distribution $q_3(d)$, with the characteristic diameters d_{10}, d_{50}, and d_{90}.

Fig. 3. SEM micrograph of initial Fe_2O_3 particles.

this rationale, the superficial gas velocity was selected as the highest practicable velocity that still prevents significant particle discharge from the reactor. It was approximately 10 times the estimated minimum fluidization velocity under cold gas conditions, corresponding to about 30 times the minimum fluidization velocity when accounting for gas expansion at the reaction temperature. This ratio is of the same order as reported in the pilot-scale FBR study [19]. The slightly higher value was chosen as an additional safety margin for the smaller XAS reactor geometry, where wall effects more strongly affect fluidization stability.

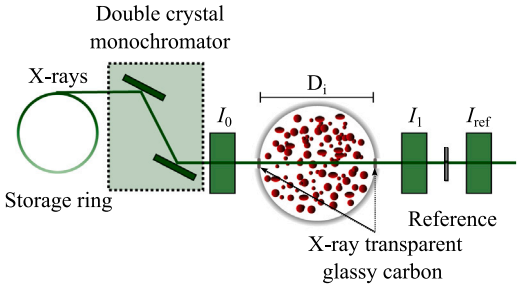

Fig. 4. Schematic of the X-ray beam path used for *operando* XAS in the FBR.

Stable fluidization was monitored by pressure drop sensing throughout the experiment, with the pressure drop profile reproducing the characteristic trends reported by Seitz et al. [19]. The experiment was run for 120 min to ensure full reduction. The selected conditions therefore provide a well-defined reference case for demonstrating the capability of *operando* XAS to track iron (oxide) phase evolution in real time during reduction with H_2 under FBR operation.

2.3. Ex situ powder analysis

Powder X-ray diffractograms were recorded using an X-ray diffractometer equipped with Cu-Kα radiation (Cu-Kα_1 = 1.5406 Å) and a Ni filter, as reported in [19]. The scans were acquired with a step size of 0.017° over a 2θ range of 10° to 100°. The XRD reflections were compared with reference data and evaluated following the procedure described in [19].

2.4. Time-resolved solid phase analysis

In situ XAS at the Fe K-edge was employed to temporally resolve the reduction of iron oxide particles with H_2 in the FBR. Time-resolved spectra capture the progressive transformation of Fe_2O_3 through Fe_3O_4 to metallic Fe, reflecting the evolving electronic structure and local coordination in real time.

XAS at the Fe K-edge provides element-specific sensitivity to oxidation state and local environment [32,33]. The energy position and fine structure of the absorption edge therefore allow differentiation between metallic and the differently oxidized iron species.

In this study, *in situ* XAS was conducted in transmission mode. According to the Lambert–Beer law, the energy-dependent absorption coefficient $\mu(E)$ is derived from the incident and transmitted intensities I_0 and I_1 via

$$\mu(E)\, D_i = \ln\left(I_0\, I_1^{-1}\right), \tag{3}$$

where D_i denotes the optical path length, *i.e.*, the inner diameter of the FBR, see Fig. 1.

The experiments were carried out at beamline P64 (DESY) [34] using a quick-scanning extended X-ray absorption fine structure (QEXAFS) monochromator [35] operated at 1 Hz. Two ionization chambers recorded I_0 and I_1, while a passivated implanted planar silicon (PIPS) diode measured a simultaneously transmitted reference signal through an Fe foil for continuous energy calibration and drift correction. The X-ray beam path through the fluidized bed, including the detector arrangement used for transmission XAS measurements, is illustrated in Fig. 4.

The heterogeneous distribution of particles and gas bubbles can deviate from the homogeneous medium implicit in the Lambert–Beer law under bubbly fluidization. However, in hard X-ray absorption spectroscopy measured in transmission mode, scattering contributions

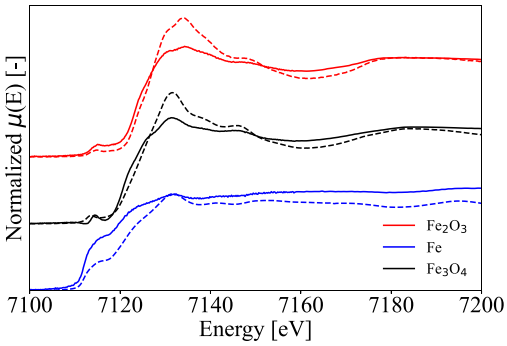

Fig. 5. XAS spectra at the Fe K-edge used as reference spectra for the LCA, *i.e.*, to decompose the recorded *operando* spectra into the temporal evolution of the corresponding molar phase fractions. Solid lines represent the spectra extracted by MCR-ALS. Dashed lines indicate the corresponding reference spectra of well-defined phases recorded with the same beamline optics. For clarity, spectra are vertically offset along the ordinate.

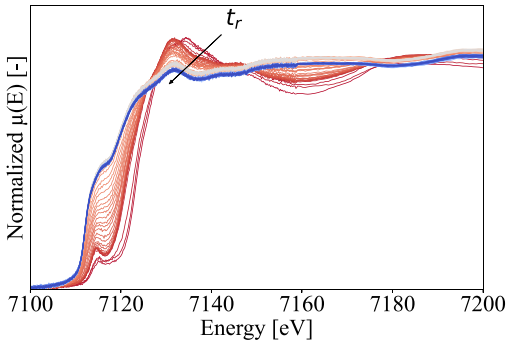

Fig. 6. XAS spectra recorded during the reduction experiment. The spectral shape evolves from Fe_2O_3 via Fe_3O_4 to metallic Fe. This progression is reflected by the color scale, which changes from red (Fe_2O_3) to blue (Fe). The spectra used as internal references for LCA, are shown in Fig. 5.

are effectively canceled out during averaging, and the remaining inhomogeneity effect manifests as spectral dampening of X-ray absorption near edge structure (XANES) features scaling with average particle size. As long as the particle size does not change substantially during the experiment, this dampening remains approximately constant, and its effect on the relative spectral shapes used for LCA is therefore limited [36]. In addition to this microscopic particle size-related effect, bubbly fluidization introduces spatial and temporal averaging due to the heterogeneous gas–solid distribution. The recorded spectra represent an integral measurement over the X-ray transmission path and across the approximately 1 mm wide Gaussian beam profile. During the 1 Hz QEXAFS acquisition, transient changes in the gas–solid distribution are averaged in the recorded spectrum, yielding reproducible spectral signals, as confirmed by the absence of erratic jumps between consecutive spectra. The quantitative analysis was then performed on spectra averaged over 1 min intervals, which effectively results in very stable spectra without any discernible particle movement-induced artifacts.

To account for inhomogeneities and the associated dampening in the XAS data analysis, the initial and final solid-state phase compositions were determined by *ex situ* X-ray diffraction (XRD) analysis, as described in Section 2.3. XRD of the as-received powder confirmed Fe_2O_3 as the initial phase. After completion of the reduction, Rietveld refinement showed that the final solid product consisted of approximately 0.99 molar fraction of metallic Fe, with a minor residual fraction of about 0.01 Fe_3O_4 and only traces of Fe_2O_3. These experimentally confirmed boundary states were used to guide the extraction of internal reference spectra from the time-resolved *operando* XAS dataset. The first and last spectra were used directly as reference spectra for Fe_2O_3 and Fe, respectively. The reference spectrum for Fe_3O_4 was derived using the built-in multivariate curve resolution–alternating least-squares (MCR-ALS) algorithm implemented in Fastosh [37]. These extracted spectra were subsequently used as reference spectra in the LCA to decompose the recorded *operando* spectra into the temporal evolution of the corresponding molar phase fractions. Fig. 5 compares the internal reference spectra extracted by MCR-ALS from the *operando* FBR dataset with external reference spectra of well-defined Fe_2O_3, Fe_3O_4, and Fe recorded with the same beamline optics but without FBR-induced dampening.

The line-of-sight (LOS) probing height was selected at L_{LOS} = 190 mm based on vertical XAS scans performed prior to the reduction experiments under FBR conditions. These scans identified this position as the best compromise between sufficient X-ray attenuation for well-defined spectral features and avoidance of excessive absorption losses. As the LOS was located in the freeboard region, the probed particle ensemble may differ from the bulk bed material, and a moderate size-selective bias toward finer particles cannot be excluded.

2.5. Time-resolved gas-phase analysis

Time-resolved gas-phase composition was monitored using a Hiden ExQ QMS. The system employed electron impact ionization. Ion currents were detected via a combined Faraday cup and secondary electron multiplier, providing high dynamic range for light gas quantification. The species analyzed were H_2 (m/z = 2), H_2O (m/z = 18), and N_2 (m/z = 28). For this purpose, a partial gas stream was extracted directly from the reactor outlet through a heated capillary line maintained at 423 K and passed through a particle filter before entering the high-vacuum sampling interface. This setup prevented condensation and minimized transport-related signal distortion. Based on the capillary geometry and applied flow rate, the gas transport delay was estimated to be in the order of one minute and was accounted for by temporal alignment of the QMS and XAS signals. Data acquisition at 59 Hz was synchronized with *in situ* XAS measurements, enabling correlation between gas- and solid-phase evolution.

3. Results and discussion

Fig. 6 shows XAS spectra recorded during the reduction experiment. The spectra gradually evolve from Fe_2O_3 at the beginning to metallic Fe, indicating progressive reduction with increasing residence time t_r. This evolution becomes evident when comparing the spectral shapes with the reference spectra shown in Fig. 5.

The molar fractions of iron (oxide) phases quantified via LCA during reduction are shown in Fig. 7, together with the simultaneously measured gas-phase composition, *i.e.*, H_2, H_2O, and N_2, obtained by QMS; additional MCR-ALS analysis including FeO as a potential phase indicated no detectable FeO accumulation under the selected reduction conditions. The Fe_2O_3 fraction decreases sharply at the onset of the reaction, accompanied by a concurrent rise in Fe_3O_4 and metallic Fe, indicating a fast initial reduction step. As the reaction proceeds, the gradient decreases markedly, which is consistent with the formation of passivating Fe and Fe_3O_4 surface layers illustrated in Fig. 8, hindering H_2 access to and diffusion of formed H_2O away from the particle core. This behavior is consistent with a gradual shift from a kinetically limited regime toward diffusion limitation [1,31]. In the gas phase, these phase changes are mirrored by an initially steep increase in the H_2O signal, which then approaches a quasi-steady state as surface passivation develops. Toward the end of the experiment, the decrease in H_2O confirms the depletion of reducible oxides and the completion of metallization.

The reduction degree $X(t_r)$, calculated from solid-phase transformation data derived via XAS, increases rapidly during the reaction. At a residence time of 28 min, XAS indicates a reduction degree of

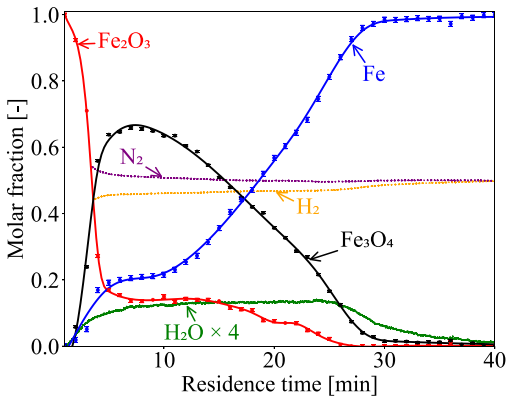

Fig. 7. Real-time tracking of iron oxide phase transformations via *in situ* XAS, along with quantification of the gas-phase composition via QMS during the reduction of micron-sized Fe_2O_3 particles.

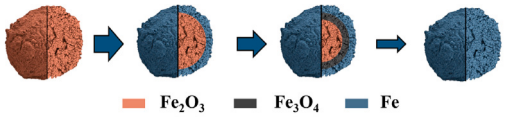

Fig. 8. Schematic of the proposed reduction mechanism, modified from [1].

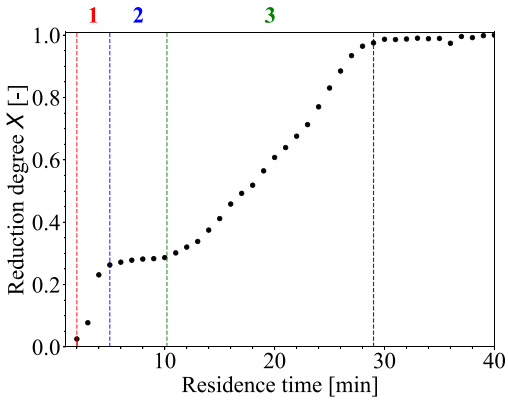

Fig. 9. Reduction degree X as a function of residence time t_r, derived from *in situ* XAS phase fractions. Vertical dashed lines indicate transitions between three qualitatively distinct kinetic regimes.

approximately 0.96. However, the reduction degree derived from gas-phase data measured by QMS is about 0.80 at the same nominal residence time. This difference reflects a temporal offset between the solid-state signal measured in the bed and the gas-phase signal detected at the reactor outlet. First, even after accounting for the instrumental gas transport delay, the reduction degree inferred from the H_2O signal remained delayed relative to the solid-phase evolution on the time scale of tens of minutes, indicating that this delay cannot be explained by gas transport through the sampling line alone. Second, QMS integrates over the entire reactor outlet, whereas XAS probes only a defined region within the FBR. Given that the LOS of *in situ* XAS was located in the freeboard region, the probed particle ensemble may not fully represent the bulk bed material. Under bubbling fluidization, particles are continuously projected above the bed surface by bubble eruption and may temporarily enter the LOS rather than being permanently elutriated. Nevertheless, smaller particles are more likely to reach this region, and a moderate bias toward finer particles can therefore not be excluded. Such a bias could also contribute to the faster apparent solid-phase conversion observed by XAS compared with the gas-phase response, though likely not to a large extent. Third, temporary trapping of H_2O formed during reduction within the porous particle structure may contribute to the observed offset. A similar behavior was reported by Spielmann et al. who observed water trapping in reduced iron oxide samples using Mössbauer spectroscopy [25]. This effect could contribute to the temporal offset between gas-phase and solid-phase data and was consistently observed throughout this and other experiments.

The time-resolved reduction degree $X(t_r)$, derived from the XAS phase fractions and shown in Fig. 9, further illustrates the temporal evolution of the reduction process and is consistent with a sequential reduction mechanism. To characterize the kinetics in the individual regimes, the Avrami exponents were determined for the three main conversion intervals, following the procedure of Stevens et al. [38], who applied the method proposed by Hancock and Clark [39]. The resulting exponents $n_1 \approx 2.87$, $n_2 \approx 0.14$, and $n_3 \approx 2.12$ for Regimes 1–3, respectively, shown in Fig. 9, are in line with the qualitative picture derived from $X(t_r)$. They indicate distinct kinetic regimes, comprising a fast initial stage, a strongly slowed intermediate stage, and an accelerated late-stage conversion.

Compared to previous studies in fixed bed reactors, the reduction observed in this work proceeds significantly faster, which can be attributed to the high H_2 concentration, *i.e.*, a 1:1 mixture of H_2/N_2, and the enhanced mass transfer under FBR conditions. In contrast to our previous FBR study [19], the present results indicate a slightly accelerated reduction. This discrepancy may partly arise from differences in probed reactor region as well as from the transient thermal conditions during the heating phase. Nielsen et al. [24] performed *in situ* XRD experiments in a capillary fixed bed reactor using only 1.4% H_2 and iron oxide nanoparticles. They reported slow kinetics, requiring about 8 h at 773 K for complete reduction. Their results nonetheless confirmed an immediate transformation from Fe_2O_3 to Fe_3O_4, consistent with the initial reduction stage identified here, but also highlighted the strong passivating effect of Fe_3O_4 and Fe surface layers — likely even more pronounced for nanoparticles with their higher specific surface area. Braun et al. [1] likewise investigated micron-sized particles in a capillary fixed bed configuration via temperature-programmed reduction experiments and observed the transient formation of Fe_3O_4 with a maximum molar fraction of 0.44. In comparison, the maximum Fe_3O_4 fraction of approximately 0.66 obtained in the present FBR study points to a stronger build-up of the magnetite intermediate, despite the overall faster reduction. Ma et al. [31] investigated the reduction of iron oxide pellets with pure H_2 at 973 K and observed a similarly rapid initial reduction of Fe_2O_3. At this higher temperature, the formation of thermodynamically stable FeO impeded further reduction. Their results also revealed the development of a passivating iron layer on the particle surface. Similar reduction behavior has also been reported for micron-sized iron oxide particles reduced with H_2, see, *e.g.*, Stevens et al. [38] and Frâdet et al. [28].

Recent investigations carried out in fluidized bed reactors further support a rapid initial reduction stage under conditions of efficient gas–solid contact. Jezernik et al. [40] demonstrated, based on *in situ* XRD and SEM, that reduction of iron ore fines with H_2 in a small-scale fluidized bed reactor operated under dynamically varying temperature conditions can reach complete conversion within short residence times. This behavior highlights the intrinsically fast reduction of Fe_2O_3 and Fe_3O_4 under fluidized bed conditions and is qualitatively consistent with the rapid early-time decay of Fe_2O_3 observed in the present work. Ren et al. [41] likewise employed a micro-scale FBR and showed that even small amounts of water vapor in the H_2-containing gas can significantly slow down the reduction of iron ore, particularly at low temperatures such as 773 K, even though this inhibiting effect diminishes at higher temperatures [38]. This sensitivity to H_2O is consistent with the pronounced plateau and the persistence of iron oxide phases observed in the present FBR experiments and suggests that locally accumulated water vapor within partially passivated Fe/Fe_3O_4 shells may contribute to the late-stage deceleration of the overall reduction.

4. Summary, concluding remarks and outlook

In this study, micron-sized iron oxide particles were probed by *in situ* XAS during reduction with H_2 in a newly designed XAS-compatible FBR operated under isothermal conditions relevant to practical operation. Combined with QMS, this approach enables simultaneous monitoring of solid- and gas-phase transformations and reveals that the reduction of micron-sized Fe_2O_3 particles with H_2 at 773 K proceeds sequentially via $Fe_2O_3 \longrightarrow Fe_3O_4 \longrightarrow Fe$. The formation of passivating Fe and/or Fe_3O_4 shells likely limits H_2 access to the particle core and the transport of H_2O formed in the particle core to the gas phase. This behavior is consistent with a gradual shift from a kinetically limited regime toward increasing diffusion and transport limitation, reflected in the pronounced plateau and the slow consumption of the remaining oxide phases at high overall conversion.

Simultaneous gas-phase analysis links these solid-state transformations directly to the transient formation of H_2O. The initially steep increase in the H_2O signal, followed by quasi-steady levels, reflects the rapid early reduction and the subsequent slowing of oxide conversion. The systematic offset between the reduction degrees derived from XAS and QMS likely arises from the different ensembles probed by both diagnostics: XAS probes particles temporarily present in the freeboard region, potentially biased toward smaller and faster-reducing particles, whereas QMS captures the overall H_2O formation from the entire reacting particle ensemble. Temporary retention of H_2O within the porous particle structure may further contribute to the delayed gas-phase response, consistent with observations by Spielmann et al. [25]. Compared with fixed bed configurations reported in the literature, the overall reduction observed here proceeds significantly faster, which can be attributed to enhanced particle mixing and improved gas–solid mass transfer characteristic of FBRs.

Beyond these mechanistic insights, the present work establishes an experimental framework for synchrotron-based *operando* investigations of iron oxide reduction in a downscaled pilot-scale FBR. The approach enables simultaneous and correlated monitoring of solid-phase transformations via XAS and gas-phase composition via QMS, providing a correlated data set for resolving the reaction dynamics in fluidized bed reactors.

Building on this foundation, upcoming studies will investigate the influence of particle morphology, PSD, and initial oxide phase, as well as the effects of temperature and H_2 concentration on the reduction dynamics. Particular attention will be given to the evolving particle morphology during reduction, including the development of porous iron particles, internal pore networks, and passivating surface layers, which are known to strongly affect reduction kinetics and mass transport within the particles [7,19,42,43]. Systematic *operando* studies under well-controlled fluidized bed conditions will therefore provide a consistent experimental basis for refining kinetic rate parameters and improving mechanistic models. Experimentally validated kinetics will enable the development of multi-scale reactor models coupling intrinsic reaction kinetics with fluidized bed hydrodynamics, gas–solid mass transfer, and particle–particle interactions, thereby supporting the design and optimization of reactors for carbon-free energy carriers based on the Fe-H_2 redox cycle for renewable energy storage.

CRediT authorship contribution statement

Martin P. Kannengießer: Writing – original draft, Visualization, Software, Investigation, Formal analysis, Data curation. **Lukas Braun:** Writing – review & editing, Investigation, Formal analysis. **Fabian P. Hagen:** Writing – original draft, Project administration, Investigation, Conceptualization. **Malte Seitz:** Writing – review & editing, Investigation. **Leon Mögerle:** Writing – review & editing, Investigation. **Björn Stelzner:** Writing – review & editing, Project administration. **Jan-Dierk Grunwaldt:** Writing – review & editing, Supervision, Funding acquisition. **Dmitry E. Doronkin:** Writing – review & editing, Project administration, Investigation, Conceptualization. **Dimosthenis Trimis:** Writing – review & editing, Supervision, Funding acquisition.

Declaration of competing interest

The authors declare that they have no known competing financial interests or personal relationships that could have appeared to influence the work reported in this paper.

Acknowledgments

The authors gratefully acknowledge funding from the German Research Foundation under the project *Reduction Behavior of Oxidized Iron Particles used as Energy Storage Material* (#558715615). In addition, this work received funding within the Clean Circles cluster project, supported by the Strategy Fund of the KIT Presidium. It also contributes to the Helmholtz Association's MTET program Resource and Energy Efficiency, Anthropogenic Carbon Cycle (#38.05.01) and to the project BOY-200 funded by the Friedrich and Elisabeth Boysen Foundation. The authors thank the Laboratory for Electron Microscopy and the Institute of Mechanical Process Engineering and Mechanics, both at KIT, for acquiring the SEM image and measuring the initial particle size distribution. We acknowledge DESY (Hamburg, Germany), a member of the Helmholtz Association HGF, for the provision of experimental facilities. Parts of this research were carried out at PETRA III. Data was collected using P64 beamline operated by DESY Photon Science. The authors thank Marc Viehweger, Dr. Aleksandr Kalinko and Dr. Wolfgang Caliebe for their assistance during the experiments. The beamtime was allocated for the proposal I-20240888.

References

[1] L. Braun, J. Spielmann, D.E. Doronkin, C. Kuhn, A. Maliugin, D.I. Sharapa, I. Huck, J. Bao, S. Tischer, F. Studt, O. Deutschmann, U.I. Kramm, J.-D. Grunwaldt, Following the structural changes of iron oxides during reduction under transient conditions, ChemSusChem 17 (24) (2024) e202401045.

[2] J.M. Bergthorson, Recyclable metal fuels for clean and compact zero-carbon power, Prog. Energy Combust. Sci. 68 (2018) 169–196.

[3] L.C. Thijs, E.M. Kritikos, A. Giusti, G. Ramaekers, J.A. van Oijen, P. de Goey, X. Mi, On the surface chemisorption of oxidizing fine iron particles: Insights gained from molecular dynamics simulations, Combust. Flame 254 (2023) 112871.

[4] J. Neumann, Q. Fradet, A. Scholtissek, F. Dammel, U. Riedel, A. Dreizler, C. Hasse, P. Stephan, Thermodynamic assessment of an iron-based circular energy economy for carbon-free power supply, Appl. Energy 368 (2024) 123476.

[5] C. Kuhn, A. Düll, P. Rohlfs, S. Tischer, M. Börnhorst, O. Deutschmann, Iron as recyclable energy carrier: Feasibility study and kinetic analysis of iron oxide reduction, Appl. Energy Combust. Sci. 12 (2022) 100096.

[6] P. Debiagi, R. Rocha, A. Scholtissek, J. Janicka, C. Hasse, Iron as a sustainable chemical carrier of renewable energy: Analysis of opportunities and challenges for retrofitting coal-fired power plants, Renew. Sustain. Energy Rev. 165 (2022) 112579.

[7] C. Kuhn, A. Knapp, M.P. Deutschmann, J. Spielmann, S. Tischer, U.I. Kramm, H. Nirschl, O. Deutschmann, Iron as recyclable metal fuel: Unraveling oxidation behavior and cyclization effects through thermogravimetric analysis, wide-angle X-ray scattering and mössbauer spectroscopy, ChemSusChem 17 (15) (2024) e202400351.

[8] W. Prasidha, N. Stevens, M. Baigmohammadi, G. Finotello, Y. Shoshin, P. de Goey, Exploring consecutive cycles of iron powder combustion for sustainable thermal energy, Combust. Flame 283 (2026) 114582.

[9] M. Sohrabi, B. Ghobadian, G. Najafi, W. Prasidha, M. Baig, P. de Goey, Iron powder particles as a clean and sustainable carrier: Investigating their impact on thermal output, Process. Saf. Env. Prot. 188 (2024) 957–969.

[10] J. Janicka, P. Debiagi, A. Scholtissek, A. Dreizler, B. Epple, R. Pawellek, A. Maltsev, C. Hasse, The potential of retrofitting existing coal power plants: A case study for operation with green iron, Appl. Energy 339 (2023) 120950.

[11] J. Neumann, R.C. da Rocha, P. Debiagi, A. Scholtissek, F. Dammel, P. Stephan, C. Hasse, Techno-economic assessment of long-distance supply chains of energy carriers: Comparing hydrogen and iron for carbon-free electricity generation, Appl. Energy Combust. Sci. 14 (2023) 100128.

[12] A. Dolai, G. Finotello, X. Mi, Assessment of H_2-air and CH_4/H_2-air fuel-rich premixed flames for flash reduction of magnetite particles, Fuel 404 (2026) 136202.

[13] Y. Qu, L. Xing, C. Wang, L. Shao, Z. Zou, Kinetic characterization of flash reduction process of hematite ore fines under hydrogen atmosphere, Int. J. Hydrog. Energy 45 (56) (2020) 31481–31493.

[14] H. Wang, H.Y. Sohn, Hydrogen reduction kinetics of magnetite concentrate particles relevant to a novel flash ironmaking process, Met. Mater. Trans. B 44 (1) (2013) 133–145.

[15] H.Y. Sohn, Y. Mohassab, Development of a novel flash ironmaking technology with greatly reduced energy consumption and CO_2 emissions, J. Sustain. Met. 2 (3) (2016) 216–227.
[16] C.J.M. Hessels, D.W.J. Lelivelt, N.C. Stevens, Y. Tang, N.G. Deen, G. Finotello, Minimum fluidization velocity and reduction behavior of combusted iron powder in a fluidized bed, Fuel 342 (2023) 127710.
[17] C. Kuhn, M. Kirn, S. Tischer, O. Deutschmann, Micron-sized iron particles as energy carrier: Cycling experiments in a fixed-bed reactor, Proc. Combust. Inst. 40 (1) (2024) 105207.
[18] H. Lee, S. Yoon, S. Kim, Y. Lee, S. Shin, S.H. Son, Fundamental modeling of a multistage fluidized bed reactor for hydrogen-based iron ore reduction, Chem. Eng. J. 511 (2025) 161755.
[19] M. Seitz, M.P. Kannengießer, B. Stelzner, F.P. Hagen, L. Braun, J. Kaltenbach, K. Märkle, M. Peterlechner, J. Spielmann, D.E. Doronkin, M.P. Deutschmann, J.-D. Grunwaldt, Y.M. Eggeler, U.I. Kramm, H. Nirschl, D. Trimis, Reduction of micron-sized iron oxide particles with high initial porosity in a fluidized bed reactor using hydrogen: Morphology and phase analysis, Fuel 405 (2026) 136422.
[20] N. Srinivasan, S. L.-I., A theoretical analysis of the fluidized-bed process for the reduction of iron ores, Chem. Eng. Sci. 45 (5) (1990) 1253–1265.
[21] D. Spreitzer, J. Schenk, Fluidization behavior and reducibility of iron ore fines during hydrogen-induced fluidized bed reduction, Particuology 52 (2020) 36–46.
[22] C.J.M. Hessels, A.H.J. Smeets, G. Finotello, N.G. Deen, Y. Tang, Sintering behavior of combusted iron powder in a packed bed reactor with nitrogen and hydrogen, Particuology 83 (2023) 8–17.
[23] D. Spreitzer, J. Schenk, Reduction of iron oxides with hydrogen—A review, Steel Res. Int. 90 (10) (2019) 1900108.
[24] M.R. Nielsen, A.B. Moss, A.S. Bjørnlund, X. Liu, A. Knop-Gericke, A.Y. Klyushin, J.-D. Grunwaldt, T.L. Sheppard, D.E. Doronkin, A. Zimina, T.E.L. Smitshuysen, C.D. Damsgaard, J.B. Wagner, T.W. Hansen, Reduction and carburization of iron oxides for Fischer–Tropsch synthesis, J. Energy Chem. 51 (2020) 48–61.
[25] J. Spielmann, F. Heck, E. Bruder, M.P. Deutschmann, E. Müller, M. Seebach, D. Braig, A. Streck, A. Scholtissek, M. Rose, Y.M. Eggeler, H. Nirschl, F. Reinauer, K. Hofmann, B. Albert, U.I. Kramm, Iron as energy carrier – Mechanistics of iron oxidation and iron oxide reduction deduced from In Situ techniques, Chem. Mater. 37 (17) (2025) 6485–6499.
[26] G. Munteanu, L. Ilieva, D. Andreeva, Kinetic parameters obtained from TPR data for α-Fe_2O_3 and Auα-Fe_2O_3 systems, Thermochim. Acta 291 (1) (1997) 171–177.
[27] E. Salucci, A. D'Angelo, V. Russo, H. Grénman, H. Saxén, Modelling of iron oxide reduction with hydrogen in a small fixed bed, Chem. Eng. Sci. 292 (2024) 119934.
[28] Q. Fradet, M. Kurnatowska, U. Riedel, Thermochemical reduction of iron oxide powders with hydrogen: Review of selected thermal analysis studies, Thermochim. Acta 726 (2023) 179552.
[29] M. Gallwitz, J. Roth, R. Breitbach, M. Jahn, G. Herz, E. Reichelt, Time-efficient method for the kinetic characterization of iron ore feedstocks for H_2-based direct reduction, J. Clean. Prod. 522 (2025) 146323.
[30] J. Spielmann, D. Braig, A. Streck, T. Gustmann, C. Kuhn, F. Reinauer, A. Kurnosov, O. Leubner, V. Potapkin, C. Hasse, O. Deutschmann, B.J.M. Etzold, A. Scholtissek, U.I. Kramm, Exploring the oxidation behavior of undiluted and diluted iron particles for energy storage: Mössbauer spectroscopic analysis and kinetic modeling, Phys. Chem. Chem. Phys. 26 (17) (2024) 13049–13060.
[31] Y. Ma, I.R. Souza Filho, X. Zhang, S. Nandy, P. Barriobero-Vila, G. Requena, D. Vogel, M. Rohwerder, D. Ponge, H. Springer, D. Raabe, Hydrogen-based direct reduction of iron oxide at 700°C: Heterogeneity at pellet and microstructure scales, Int. J. Min. Met. Mater. 29 (10) (2022) 1901–1907.
[32] A. Boubnov, H. Lichtenberg, S. Mangold, J.-D. Grunwaldt, Identification of the iron oxidation state and coordination geometry in iron oxide- and zeolite-based catalysts using pre-edge XAS analysis, J. Synchrotron Radiat. 22 (2) (2015) 410–426.
[33] B.B. Sarma, J.-D. Grunwaldt, Operando spectroscopy to understand dynamic structural changes of solid catalysts, Chimia 78 (5) (2024) 288–296.
[34] W.A. Caliebe, V. Murzin, A. Kalinko, M. Görlitz, High-flux XAFS-beamline P64 at PETRA III, AIP Conf. Proc. 2054 (1) (2019) 060031.
[35] B. Bornmann, J. Kläs, O. Müller, D. Lützenkirchen-Hecht, R. Frahm, The quick EXAFS setup at beamline P64 at PETRA III for up to 200 spectra per second, AIP Conf. Proc. 2054 (1) (2019) 040008.
[36] J. Timoshenko, D. Kordus, J.K. Mathiesen, U. Hejral, P. Zeller, G. Behrendt, E. Öztuna, J. Wang, Z. Gheisari, R. Eckert, S. Reitmeier, A. Reitzmann, H. Ruland, J. Folke, T. Lunkenbein, B. Roldan Cuenya, X-ray absorption by a microgranular sample, Phys. Rev. B 112 (2) (2025) 024105.
[37] G. Landrot, E. Fonda, Fastosh: A software for the treatment of XAFS datasets of environmental relevance or acquired in operando conditions, J. Synchrotron Radiat. 32 (4) (2025) 1085–1094.
[38] N.C. Stevens, A. Dolai, C.J.M. Hessels, N.G. Deen, G. Finotello, Hydrogen reduction of combusted iron powder: Role of water vapor in reaction kinetics, Powder Technol. 469 (2026) 121912.
[39] J.D. Hancock, J.H. Sharp, Method of comparing solid-state kinetic data and its application to the decomposition of kaolinite, brucite, and $BaCO_3$, J. Am. Ceram. Soc. 55 (2) (1972) 74–77.
[40] S. Jezernik, D. Matulka, G. Friedbacher, M. Berchtold, F. Winter, Investigation of structural changes during hydrogen-based direct reduction of iron ore fines under pressure using in-situ XRD and SEM, J. Env. Chem. Eng. 13 (6) (2025) 120312.
[41] S. Ren, L. Wang, J. Zhang, S. Li, Effect of H_2O(g) on the hydrogen reduction of iron ore in fluidized bed, Fuel 405 (2026) 136647.
[42] X. Zhang, S. He, H. Sun, Q. Zhu, J. Li, H. Li, Mechanism of surface morphology evolution in the reduction of fine iron ore in a conical fluidized bed reactor, Chem. Eng. Sci. 220 (2020) 115468.
[43] X. Gong, B. Zhang, Z. Wang, Z. Guo, Insight of iron whisker sticking mechanism from iron atom diffusion and calculation of solid bridge radius, Metall. Mater. Trans. B 45 (6) (2014) 2050–2056.